Localization supervision of chest x-ray classifiers using label-specific eye-tracking annotation

Ricardo Bigolin Lanfredi[1], Joyce D. Schroeder[2], and Tolga Tasdizen[1]

[1] Scientific Computing and Imaging Institute, University of Utah, 72 S Central Campus Drive, Room 3750, Salt Lake City, UT 84112, USA
ricbl@sci.utah.edu
[2] Department of Radiology and Imaging Sciences, University of Utah, 30 North 1900 East #1A071, Salt Lake City, UT 84132, USA

Abstract. Convolutional neural networks (CNNs) have been successfully applied to chest x-ray (CXR) images. Moreover, annotated bounding boxes have been shown to improve the interpretability of a CNN in terms of localizing abnormalities. However, only a few relatively small CXR datasets containing bounding boxes are available, and collecting them is very costly. Opportunely, eye-tracking (ET) data can be collected in a non-intrusive way during the clinical workflow of a radiologist. We use ET data recorded from radiologists while dictating CXR reports to train CNNs. We extract snippets from the ET data by associating them with the dictation of keywords and use them to supervise the localization of abnormalities. We show that this method improves a model's interpretability without impacting its image-level classification.

Keywords: Eye tracking · Chest x-ray · Interpretability

1 Introduction

Along with the success of deep learning methods in medical image analysis, interpretability methods have been used to validate that models are working as expected [15]. The interpretability of deep learning models has also been listed as a critical research priority for artificial intelligence in medical imaging [10]. The employment of bounding box annotations during training has been shown to improve a model's ability to highlight abnormalities and, consequently, their interpretability [12]. However, bounding boxes for medical images are costly to acquire since they require expert annotation, whereas image-level labels can readily be extracted from radiology reports. This fact is exemplified by the relatively small size of bounding box datasets for chest x-rays (CXRs) [13,19] when compared to the size of CXR datasets with image-level labels. Eye-tracking (ET) data, on the other hand, contain implicit information about the location of labels, and its collection can potentially be scaled up if the acquisition of gaze from radiologists is implemented in clinical practice.

We propose to use ET data with timestamped dictations of radiology reports to identify when the presence of specific abnormalities was dictated and extract

the associated gaze locations. The extracted information can then be used as label-specific annotation for supervising models to highlight abnormalities spatially. The localization supervision is performed using a multiple instance learning loss over the last spatial layer of a convolutional neural network (CNN) [12]. To complement the annotations of an ET dataset, we employ a large dataset of CXRs with image-level labels in a weak supervision formulation. We evaluate the classification performance and, using the grid output of the network to extract visual attribution heatmaps, the ability to localize abnormalities of a model trained with data annotated by ET. This model is compared against baselines using no annotated data and hand-annotated data. We show that using ET data during training improves the localization performance of generated interpretable heatmaps without compromising area under the receiver operating characteristic curve (AUC) classification scores and that this type of data can potentially replace hand-labeling.

Other studies have applied ET data for localizing abnormalities and improving the localization of models. Stember et al. [18] showed that radiologists looked at the location of a label when indicating the presence of tumors in MRIs. The method we propose uses dictations to similarly identify moments when the radiologist looks at evidence of abnormality. However, we use a less restrictive and more challenging scenario, with freeform reports and multiple types of abnormalities reported. Karargyris et al. [9] trained a multitask CXR classification network with an additional output representing an ET map captured during a report dictation. Our study focuses on more complex uses of the ET data, beyond the supervision of a single ET heatmap for all labels. Saab et al. showed that, when gaze data are aggregated in hand-crafted features and used in a multitask setup, the GradCAM heatmap of a model overlaps more often with the location of abnormalities [17]. However, their study employed a dataset where radiologists focused only on finding pneumothoraces, making their ET data label-specific and their setup distant from clinical practice.

2   Methods

2.1   Extracting Localization Information from Eye-Tracking Data

We designed a pipeline to extract disease locations from ET data. This pipeline has two main parts: extracting label mentions in reports and generating an ET heatmap for a given detected label. A representation of the pipeline is shown in Figure 1. The pipeline requires the ET dataset to contain timestamps, transcriptions of report dictations, and fixations, i.e., locations in the image where radiologists stabilized their gaze for some time.

To extract labels from reports, we adopted a modified version of the CheXpert labeler [6], which uses a set of hand-crafted rules to detect label mentions and negation structures.

From observing the gaze of radiologists on a few examples, we noticed patterns that seemed to be in common for all radiologists:
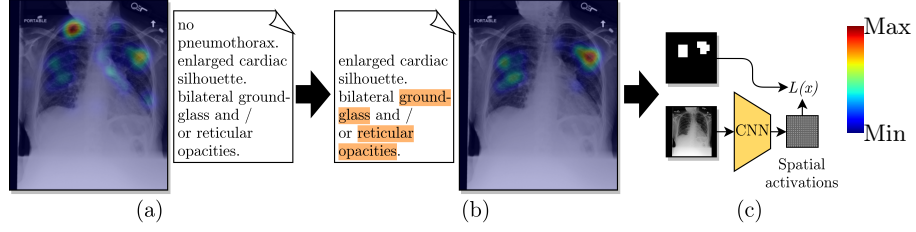
Fig. 1. Diagram of the use of ET data from a radiologist to train a CNN for improved localization. (a) The ET heatmap from the dictation of the full report. (b) Label-specific annotation for the label *Opacity*. The keywords associated with this label, found by the adapted CheXpert labeler, are highlighted in orange. The two listed sentences represent the timestamps from which fixations were extracted for generating the label-specific heatmap. (c) In the employed loss function, the activations of the spatial layers of a CNN are compared against the resized and binarized ET heatmap.

- for the first moments after being shown a CXR, radiologists looked all over the image without dictating anything;
- when dictating, radiologists usually looked at regions corresponding to the content of the current sentence or the following sentence (when near the end of the dictation of the current sentence).

From these two observations, we decided to generate ET heatmaps for detected labels from the fixations of the sentences where the label was mentioned and the previous one, with a limit of 5 seconds previous to the start of the mentioning sentence. Further clarifications are given in Figure 1a and 1b. Heatmaps were generated by placing Gaussians over each fixation location with a standard deviation of one degree of visual angle, following Le Meur et al. [11]. Fixations had the amplitude of their Gaussians weighted by their duration. The heatmap for each detected mention of a label was normalized to have a maximum value of 1. Multiple mentions of a label for the same CXR were aggregated with a maximum function.

2.2 Loss Function

We used the multiple instance learning formulation from Li et al. [12] to train CNNs with the extracted ET heatmaps. The CNNs were modified to output a grid of cells, where each cell represented a multi-label classifier for label presence in the homologous region of the image. The image-level prediction $C_k(x)$ for label k was formulated as

$$C_k(x) = 1 - \prod_{j \in \Gamma} 1 - \sigma\left(\gamma_{jk}\right), \tag{1}$$

where γ_{jk} is the logit output for class k and grid cell j, Γ is the set of all grid cells, and $\sigma(x)$ is the sigmoid function. Equation 1 is a soft version of the Boolean

OR function, assigning a positive image-level label when at least one of the grid cells was found to contain that class.

During training, the loss function depended on the presence of a localization annotation. For images annotated with localization (A), grid cells were trained to match a resized version of the annotation, as shown in Figure 1c. We used the loss

$$L_{kA}(x) = -\log \left(\prod_{j \in B} \sigma\left(\gamma_{jk}\right) \prod_{j \in \Gamma - B} 1 - \sigma\left(\gamma_{jk}\right) \right), \tag{2}$$

where B is the set of grid cells labeled as containing evidence of disease and $L_{kA}(x)$ is the loss function for annotated images of class k.

For images that did not contain localization annotations (U), the loss depended on the image-level label. For positive images, at least one grid cell should be positive. We used the loss

$$L_{kU^+}(x) = -\log\left(C_k(x)\right), \tag{3}$$

where $L_{kU^+}(x)$ is the loss function for unannotated images labeled as positive for class k. For negative images, all grid cells should be negative. We used

$$L_{kU^-}(x) = -\log \left(\prod_{j \in \Gamma} 1 - \sigma\left(\gamma_{jk}\right) \right) \tag{4}$$

where $L_{kU^-}(x)$ is the loss function for unannotated images labeled as negative for class k. The total loss function $L(x)$ to be minimized was then formulated as

$$L(x) = \mathbb{E}_{x \in X} \left[\sum_{k \in K} \lambda_A \mathbb{1}_{kA}(x) L_{kA}(x) + \mathbb{1}_{kU^+}(x) L_{kU^+}(x) + \mathbb{1}_{kU^-}(x) L_{kU^-}(x) \right], \tag{5}$$

where λ_A is a hyperparameter controlling the relative importance of annotated images during training, X is the set of all images, annotated and unannotated, K is the set of all classes, and $\mathbb{1}_{kA}(x)$, $\mathbb{1}_{kU^+}(x)$, and $\mathbb{1}_{kU^-}(x)$ are indicator functions that were 1 when the image x was annotated, positive for class k (unannotated) and negative for class k (unannotated), respectively.

Avoiding numerical underflow and balanced range normalization To avoid numerical underflow and have a more uniform range for the output of models, Li et al. [12] suggested to normalize the factors of the products in Equations 1 to 5, i.e., $\sigma(\gamma_{jk})$ and $1 - \sigma(\gamma_{jk})$, to the range $[0.98, 1]$. After running tests, we achieved better results by balancing this normalization, changing the range of each product factor to $[0.0056738^{(1/n_t)}, 1]$, where n_t is the number of factors being multiplied. This range allows for all products to have a similar expected range, and keeps the same $[0.98,1]$ range when $n_t = 256$.
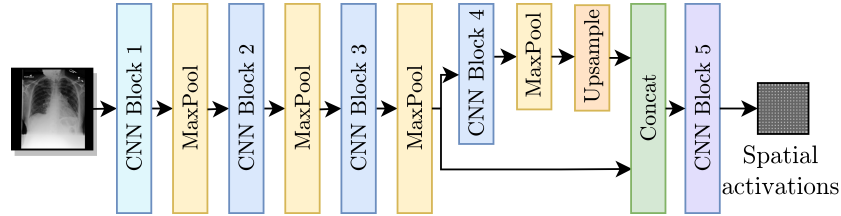
Fig. 2. Modified Resnet-50 architecture to include the multi-resolution branches

2.3 Multi-resolution Architecture

As shown in Figure 2, we adapted the Resnet-50 [4] architecture by replacing its average pooling and last linear layer with two convolutional layers separated by batch normalization [5] and ReLU activation (CNN Block 5 from Figure 2). To improve the results for labels with small findings in the original image, we modified the network such that spatial maps with 32×32 resolution were used as inputs to CNN Block 5.

3 Experiments

We used two datasets in our study. The REFLACX dataset [2,1,3] provides ET data and reports from five radiologists for CXRs from the MIMIC-CXR-JPG dataset [3,7,8]. Additionally, the REFLACX dataset contains image-level labels and radiologist-drawn abnormality ellipses, which can be used to validate the locations highlighted by our tested models. Except for the experiments described in Section 3.1, we used examples from Phase 3 of the REFLACX dataset. The MIMIC-CXR-JPG dataset, which contains patients who visited the emergency department of the Beth Israel Deaconess Medical Center between 2011 and 2016, was also utilized for its unannotated CXRs and image-level labels. Images from the MIMIC-CXR-JPG dataset were filtered using the same criteria as the REFLACX dataset: only labeled frontal images from studies with a single frontal image were considered. The test sets for both datasets were kept the same. A few subjects from the training set of the REFLACX dataset were assigned to its validation set so that around 10% of the REFLACX dataset was part of the validation set. The same subjects were also assigned to the validation set of the MIMIC-CXR-JPG dataset. The train, validation, and test splits had, respectively, 1724, 277, and 506 images for the annotated set and 187519, 4275, and 2701 images for the unannotated set. The use of both datasets did not require ethics approval because they are publicly available de-identified datasets.

The sets of labels from the annotated and unannotated datasets were different. We decided to use the ten labels listed in Table 4. In the Supplementary Material, we provide, in Table S1, a list of the labels from each dataset that were considered equivalent to each of the ten labels used in this study and, in Table S2, the number of examples of each label present in the datasets.

For our experiments[3], we used PyTorch 1.10.2 [14]. Hyperparameters commonly used for CXR classifiers were employed during training and were not tuned for any tested method. Models were trained for 60 epochs with the AMS-Grad Adam optimizer [16] using a learning rate equal to 0.001 and weight decay of 0.00001. A batch size of 20 images was chosen for the use of GPUs with 12GB of memory or more. Images were resized such that their longest dimension had 512 pixels, whereas the other dimension was padded with black pixels to reach a length of 512 pixels. For training, images were augmented with rotation up to 45 degrees, translation up to 15%, and scaling up to 15%. The grid supervised by loss $L(x)$ had 1024 cells (32×32). We used the max-pooling operation to convert the ET heatmap annotations to the same dimension. We thresholded the ET heatmaps at 0.15. This number was chosen after visual analysis of their histograms of intensities. We used $\lambda_A = 5$ following Li et al. [12]. We trained models with five different seeds and report their average results and 95% confidence intervals. Experiments were run in internal servers containing Nvidia GPUs (TITAN RTX 24GB, TITAN V 12 GB, RTX A6000 48GB, Tesla V100-SXM2 16 GB). Each training run took approximately two days in one GPU.

3.1   Labeler

Table 1. Results of the label detection with a modified version of the CheXpert labeler [6]. AMC stands for *Abnormal Mediastinal Contour* and ECS for *Enlarged Cardiac Silhouette*.

Label	Recall	Precision	Label	Recall	Precision
AMC	0.67	0.73	Interstitial Lung Disease	0.75	0.27
Acute Fracture	1.00	1.00	Lung Nodule or Mass	0.50	0.50
Atelectasis	0.87	0.64	Pleural Abnormality	0.97	0.98
Consolidation	0.96	0.77	Pneumothorax	0.89	1.00
ECS	0.91	0.92	Pulmonary Edema	0.89	0.86
Groundglass Opacity	0.79	0.75			

The set of labels from the REFLACX dataset is slightly different from the ones provided by the CheXpert labeler. With the help of a cardiothoracic subspecialty-trained radiologist, we modified the labeler to output a new set of labels. Modifications were also made to improve the identification of the already present labels after observing common mistakes on a separate validation set, composed of 20% of Phase 1 and Phase 2 from the REFLACX dataset. We adjusted rules for negation finding and added/adapted expressions to match and unmatch labels, and the final set of rules can be found in our code repository. Labeler quality estimations, after modifications, are shown in Table 1 and were calculated with

---

[3] The code for our experiments can be found at https://github.com/ricbl/eye-tracking-localization

the rest of the data from Phase 2. Results were variable depending on the label, and misdetections should be expected when using this labeler.

3.2 Location Extraction

We tested several methods for extracting label-specific localization of abnormalities from the eye-tracking data. All methods involved the accumulation of fixations into heatmaps, with different starting accumulation times, after extracting the label's mention time from the dictation. All methods ended the accumulation of fixations by the end of the mention sentence.

We compared the activation of the extracted heatmaps with the hand-annotated ellipses, as shown in Table 2. One of the highest scoring methods was the one we first proposed from our qualitative observations and is the method reported in the paper.

Table 2. Tested extraction methods for label-specific localization of abnormality.

Start time of accumulation	IoU
MAX(Start of mention sentence - 2.5s, Start of previous sentence)	0.217
MAX(Start of mention sentence - 5.0s, Start of previous sentence)	0.220
MAX(Start of mention sentence - 7.5s, Start of previous sentence)	0.220
Start of CXR reading	0.176
Start of first sentence	0.187
End of previous sentence	0.211
Start of previous sentence	0.218
Start of mention sentence	0.185

3.3 Baselines

We evaluated a model trained without the annotated data (unannotated) and a model trained with data annotated by the drawn ground truth (GT) truth ellipses. The ellipses were represented by binary heatmaps and were processed in the same way as the ET heatmaps. The loss function, CNN architecture, and training hyperparameters were the same for all methods. We did not include a cross-entropy loss baseline because it achieved lower scores than the presented methods. The best epoch for each method was chosen using the average AUC on the validation set. The best model output threshold for each method and label was calculated using the average validation intersection over union (IoU) over the five seeds, considering the full range of thresholds.

3.4 Evaluation

We evaluated our model and the two baselines by calculating the test AUC for image-level labels of the MIMIC-CXR-JPG dataset and the test IoU for

localization of abnormalities, compared against the drawn GT ellipses. IoU was calculated individually per positive label for all images with a positive label. To calculate the position where the model localized the abnormality, we used the grid output of the network. The outputs of the network were upscaled to the resolution of the GT ellipses using nearest-neighbor interpolation.

Table 3. Results on the test set comparing the model trained with ET data with the two baselines. AUC and IoU were averaged over the scores for each label.

Method	Unannotated	Ellipse	ET model (ours)
AUC	.770 [.765,.774]	.766 [.765,.768]	.767 [.765,.769]
IoU	.208 [.204,.212]	.255 [.254,.257]	.216 [.214,.218]

Results, averaged over all labels, are presented in Table 3. The average AUC for the model using the ET data was not significantly different from the baselines. Regarding localization, the IoU values showed that training with the ET data was significantly better than training without annotated data and worse than training with the hand-labeled localization ellipses.

Results for individual labels are presented in Tables 4 and 5. AUC was stable among all methods for almost all labels. Successful and unsuccessful heatmaps generated by our trained models are shown in Figure 3 and in Figure S1 from the Supplementary Material.

Table 4. Per-label AUC metric on the test set for the two baselines and our method.

Label	Unannotated	Ellipse	ET model (ours)
AMC	.659 [.651,.668]	.662 [.655,.669]	.662 [.654,.670]
Atelectasis	.752 [.748,.756]	.752 [.751,.753]	.752 [.751,.754]
ECS	.766 [.763,.769]	.766 [.763,.770]	.765 [.763,.768]
Consolidation	.714 [.710,.719]	.715 [.707,.723]	.717 [.711,.723]
Edema	.838 [.836,.840]	.837 [.835,.840]	.839 [.837,.841]
Fracture	.741 [.720,.762]	.721 [.701,.740]	.721 [.713,.729]
Lung Lesion	.752 [.741,.763]	.745 [.734,.757]	.747 [.734,.760]
Opacity	.786 [.783,.789]	.786 [.784,.789]	.784 [.779,.789]
Pleural abnormality	.867 [.865,.869]	.867 [.864,.869]	.868 [.863,.873]
Pneumothorax	.824 [.820,.827]	.811 [.804,.819]	.812 [.802,.823]

3.5   Ablation Study

We present in Table 6 the results of an ablation study with each modification added to the original method from Li et al. [12]. We show an advantage from each modification for all methods.

Table 5. Per-label IoU metric on the test set for the two baselines and our method.

Label	Unannotated	Ellipse	ET model (ours)
AMC	.114 [.105,.124]	.121 [.099,.144]	.138 [.127,.149]
Atelectasis	.257 [.248,.267]	.326 [.319,.333]	.275 [.266,.284]
ECS	.338 [.319,.357]	.471 [.444,.499]	.298 [.287,.309]
Consolidation	.251 [.246,.257]	.308 [.300,.316]	.265 [.260,.270]
Edema	.342 [.334,.351]	.397 [.391,.404]	.370 [.364,.376]
Fracture	.003 [.003,.003]	.006 [.001,.012]	.007 [.002,.012]
Lung Lesion	.134 [.123,.144]	.169 [.147,.191]	.159 [.149,.169]
Opacity	.274 [.271,.278]	.345 [.341,.348]	.321 [.316,.326]
Pleural abnormality	.217 [.212,.223]	.264 [.257,.271]	.215 [.210,.221]
Pneumothorax	.151 [.139,.162]	.144 [.137,.150]	.110 [.106,.114]
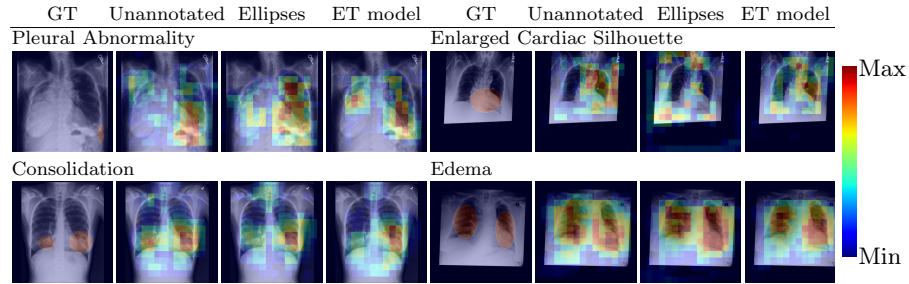
Fig. 3. Localization output for the models for random test CXRs.

4   Conclusion

We proposed a method for producing label-specific localization annotations from ET data and for training models to have spatial activations that match the annotations. We improved the interpretability of deep learning models for CXRs, as measured by comparing visual attribution heatmaps against hand-annotated localization of abnormalities, showing the potential of using this type of data for scaling up annotations.

The ET data were relatively noisy. Furthermore, the use of the fixations from two complete sentences for generating the localization annotation for a single label was necessary, given the gaze behavior of radiologists. However, it is also likely that this method caused false positives. In future work, we will investigate

Table 6. IoU metric on the test set indicating the advantage of using each of the modifications to the method proposed by Li et al. [12].

Method	Unannotated	Ellipse	ET model
Li et al. [12]	.159 [.155,.163]	.208 [.204,.211]	.185 [.181,.189]
+ Balanced Range Normalization	.164 [.160,.168]	.239 [.237,.242]	.202 [.200,.205]
+ Multi-Resolution Architecture	.208 [.204,.212]	.255 [.254,.257]	.216 [.214,.218]

other methods of extracting the localization information to reduce the noise in the data, including methods of unsupervised alignment.

References

1. Bigolin Lanfredi, R., Zhang, M., Auffermann, W., Chan, J., Duong, P., Srikumar, V., Drew, T., Schroeder, J., Tasdizen, T.: REFLACX, a dataset of reports and eye-tracking data for localization of abnormalities in chest x-rays. CoRR **abs/2109.14187** (2021), `https://arxiv.org/abs/2109.14187`
2. Bigolin Lanfredi, R., Zhang, M., Auffermann, W., Chan, J., Duong, P., Srikumar, V., Drew, T., Schroeder, J., Tasdizen, T.: REFLACX: Reports and eye-tracking data for localization of abnormalities in chest x-rays (2021). `https://doi.org/10.13026/E0DJ-8498`, `https://physionet.org/content/reflacx-xray-localization/1.0.0/`
3. Goldberger, A.L., Amaral, L.A.N., Glass, L., Hausdorff, J.M., Ivanov, P.C., Mark, R.G., Mietus, J.E., Moody, G.B., Peng, C.K., Stanley, H.E.: PhysioBank, PhysioToolkit, and PhysioNet: Components of a new research resource for complex physiologic signals. Circulation **101**(23), e215–e220 (2000). `https://doi.org/10.1161/01.CIR.101.23.e215`
4. He, K., Zhang, X., Ren, S., Sun, J.: Deep residual learning for image recognition. In: 2016 IEEE Conference on Computer Vision and Pattern Recognition, CVPR 2016, Las Vegas, NV, USA, June 27-30, 2016. pp. 770–778. IEEE Computer Society (2016). `https://doi.org/10.1109/CVPR.2016.90`
5. Ioffe, S., Szegedy, C.: Batch normalization: Accelerating deep network training by reducing internal covariate shift. In: Bach, F.R., Blei, D.M. (eds.) Proceedings of the 32nd International Conference on Machine Learning, ICML 2015, Lille, France, 6-11 July 2015. JMLR Workshop and Conference Proceedings, vol. 37, pp. 448–456. JMLR.org (2015), `http://proceedings.mlr.press/v37/ioffe15.html`
6. Irvin, J., Rajpurkar, P., Ko, M., Yu, Y., Ciurea-Ilcus, S., Chute, C., Marklund, H., Haghgoo, B., Ball, R.L., Shpanskaya, K.S., Seekins, J., Mong, D.A., Halabi, S.S., Sandberg, J.K., Jones, R., Larson, D.B., Langlotz, C.P., Patel, B.N., Lungren, M.P., Ng, A.Y.: CheXpert: A large chest radiograph dataset with uncertainty labels and expert comparison. In: The Thirty-Third AAAI Conference on Artificial Intelligence, AAAI 2019, The Thirty-First Innovative Applications of Artificial Intelligence Conference, IAAI 2019, The Ninth AAAI Symposium on Educational Advances in Artificial Intelligence, EAAI 2019, Honolulu, Hawaii, USA, January 27 - February 1, 2019. pp. 590–597. AAAI Press (2019). `https://doi.org/10.1609/aaai.v33i01.3301590`
7. Johnson, A., Lungren, M., Peng, Y., Lu, Z., Mark, R., Berkowitz, S., Horng, S.: MIMIC-CXR-JPG - chest radiographs with structured labels (version 2.0.0) (2019). `https://doi.org/10.13026/8360-t248`, `https://physionet.org/content/mimic-cxr-jpg/2.0.0/`

8. Johnson, A.E.W., Pollard, T.J., Berkowitz, S.J., Greenbaum, N.R., Lungren, M.P., Deng, C., Mark, R.G., Horng, S.: MIMIC-CXR-JPG: A large publicly available database of labeled chest radiographs. CoRR **abs/1901.07042** (2019), `https://arxiv.org/abs/1901.07042`

9. Karargyris, A., Kashyap, S., Lourentzou, I., Wu, J.T., Sharma, A., Tong, M., Abedin, S., Beymer, D., Mukherjee, V., Krupinski, E.A., Moradi, M.: Creation and validation of a chest x-ray dataset with eye-tracking and report dictation for AI development. Scientific Data **8**(1) (Mar 2021). `https://doi.org/10.1038/s41597-021-00863-5`

10. Langlotz, C.P., et al.: A roadmap for foundational research on artificial intelligence in medical imaging: From the 2018 NIH/RSNA/ACR/the academy workshop. Radiology **291**, 781–791 (2019)

11. Le Meur, O., Baccino, T.: Methods for comparing scanpaths and saliency maps: strengths and weaknesses. Behavior Research Methods pp. 1–16 (Jul 2012). `https://doi.org/10.3758/s13428-012-0226-9`, `https://hal.inria.fr/hal-00757615`

12. Li, Z., Wang, C., Han, M., Xue, Y., Wei, W., Li, L., Fei-Fei, L.: Thoracic disease identification and localization with limited supervision. In: 2018 IEEE Conference on Computer Vision and Pattern Recognition, CVPR 2018, Salt Lake City, UT, USA, June 18-22, 2018. pp. 8290–8299. IEEE Computer Society (2018). `https://doi.org/10.1109/CVPR.2018.00865`

13. Nguyen, H.Q., Lam, K., Le, L.T., Pham, H.H., Tran, D.Q., Nguyen, D.B., Le, D.D., Pham, C.M., Tong, H.T.T., Dinh, D.H., Do, C.D., Doan, L.T., Nguyen, C.N., Nguyen, B.T., Nguyen, Q.V., Hoang, A.D., Phan, H.N., Nguyen, A.T., Ho, P.H., Ngo, D.T., Nguyen, N.T., Nguyen, N.T., Dao, M., Vu, V.: Vindr-cxr: An open dataset of chest x-rays with radiologist's annotations (2021)

14. Paszke, A., Gross, S., Massa, F., Lerer, A., Bradbury, J., Chanan, G., Killeen, T., Lin, Z., Gimelshein, N., Antiga, L., Desmaison, A., Köpf, A., Yang, E., DeVito, Z., Raison, M., Tejani, A., Chilamkurthy, S., Steiner, B., Fang, L., Bai, J., Chintala, S.: PyTorch: An imperative style, high-performance deep learning library. In: Wallach, H.M., Larochelle, H., Beygelzimer, A., d'Alché-Buc, F., Fox, E.B., Garnett, R. (eds.) Advances in Neural Information Processing Systems 32: Annual Conference on Neural Information Processing Systems 2019, NeurIPS 2019, December 8-14, 2019, Vancouver, BC, Canada. pp. 8024–8035 (2019)

15. Rajpurkar, P., Irvin, J., Zhu, K., Yang, B., Mehta, H., Duan, T., Ding, D., Bagul, A., Langlotz, C., Shpanskaya, K., Lungren, M.P., Ng, A.Y.: Chexnet: Radiologist-level pneumonia detection on chest x-rays with deep learning (2017)

16. Reddi, S.J., Kale, S., Kumar, S.: On the convergence of adam and beyond. In: International Conference on Learning Representations (2018), `https://openreview.net/forum?id=ryQu7f-RZ`

17. Saab, K., Hooper, S.M., Sohoni, N.S., Parmar, J., Pogatchnik, B., Wu, S., Dunnmon, J.A., Zhang, H.R., Rubin, D., Ré, C.: Observational supervision for medical image classification using gaze data. In: Medical Image Computing and Computer Assisted Intervention - MICCAI 2021. pp. 603–614. Springer International Publishing (2021). `https://doi.org/10.1007/978-3-030-87196-3_56`

18. Stember, J.N., Celik, H., Gutman, D., Swinburne, N., Young, R., Eskreis-Winkler, S., Holodny, A., Jambawalikar, S., Wood, B.J., Chang, P.D., Krupinski, E., Bagci, U.: Integrating eye tracking and speech recognition accurately annotates MR brain images for deep learning: Proof of principle. Radiology: Artificial Intelligence **3**(1), e200047 (2021). `https://doi.org/10.1148/ryai.2020200047`

19. Wang, X., Peng, Y., Lu, L., Lu, Z., Bagheri, M., Summers, R.M.: ChestX-Ray8: Hospital-scale chest x-ray database and benchmarks on weakly-supervised classification and localization of common thorax diseases. In: 2017 IEEE Conference on Computer Vision and Pattern Recognition, CVPR 2017, Honolulu, HI, USA, July 21-26, 2017. pp. 3462–3471. IEEE Computer Society (2017). `https://doi.org/10.1109/CVPR.2017.369`

Supplementary Material

Table S1. List of labels that were grouped to form the labels from the analysis presented in this paper.

Label in our study	Labels from public datasets
Abnormal Mediastinal Contour (AMC)	abnormal mediastinal contour (AMC), enlarged cardiomediastinum
Atelectasis	atelectasis
Enlarged Cardiac Silhouette (ECS)	enlarged cardiac silhouette (ECS), cardiomegaly
Consolidation	consolidation
Edema	pulmonary edema, edema
Fracture	fracture, acute fracture
Lung Lesion	lung nodule or mass, lung lesion
Opacity	pulmonary edema, edema, lung nodule or mass, atelectasis, consolidation, groundglass opacity, interstitial lung disease, pneumonia, lung opacity
Pleural Abnormality	pleural abnormality, pleural other, pleural effusion
Pneumothorax	pneumothorax

Table S2. Number of positive examples for each of the splits for both employed datasets: REFLACX (R) and MIMIC-CXR-JPG (M).

Label	Train R	Val R	Test R	Train M	Val M	Test M
Abnormal Mediastinal Contour	59	8	27	13551	351	289
Atelectasis	503	69	189	46981	1196	754
Enlarged Cardiac Silhouette	340	55	173	41681	1138	821
Consolidation	543	95	196	12311	352	253
Edema	222	39	124	33383	971	841
Fracture	34	5	27	4028	62	71
Lung Lesion	77	13	41	6015	114	106
Opacity	865	131	337	97640	2560	1861
Pleural Abnormality	486	69	205	50914	1426	1036
Pneumothorax	48	6	13	9653	258	96
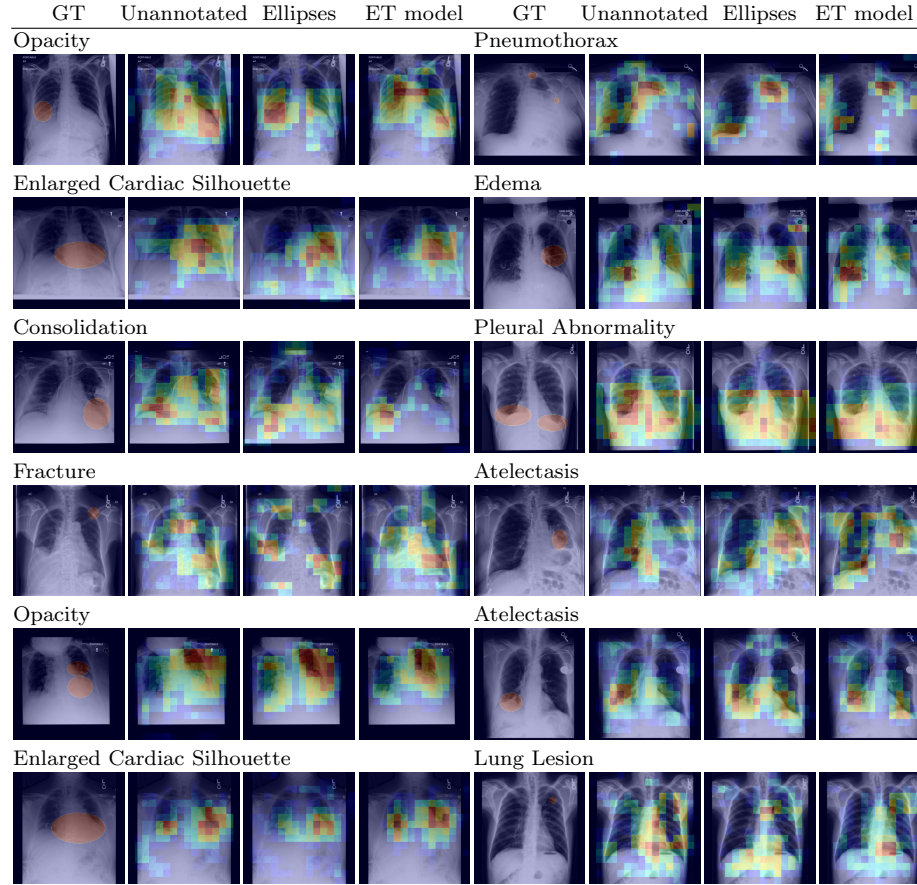
Fig. S1. Localization output for random test CXRs. For a color legend, check Figure 3.